The Astrophysical Journal, 784:29 (10pp), 2014 March 20 doi:10.1088/0004-637X/784/1/29

THE GENERATION AND DAMPING OF PROPAGATING MHD KINK WAVES IN THE SOLAR ATMOSPHERE

R. J. Morton[1], G. Verth[2], A. Hillier[3], and R. Erdélyi[2]
[1] Mathematics and Information Sciences, Northumbria University, Newcastle Upon Tyne NE1 8ST, UK; richard.morton@northumbria.ac.uk
[2] Solar Physics and Space Plasma Research Centre (SP^{2}RC), The University of Sheffield, Hicks Building, Hounsfield Road, Sheffield S3 7RH, UK; g.verth@sheffield.ac.uk, robertus@sheffield.ac.uk
[3] Kwasan and Hida Observatories, Kyoto University, 17 Ohmine-cho Kita Kazan, Yamashina-ku, Kyoto City, Kyoto 607-8471, Japan
Received 2013 September 24; accepted 2014 January 17; published 2014 February 28

ABSTRACT

The source of the non-thermal energy required for the heating of the upper solar atmosphere to temperatures in excess of a million degrees and the acceleration of the solar wind to hundreds of kilometers per second is still unclear. One such mechanism for providing the required energy flux is incompressible torsional Alfvén and kink magnetohydrodynamic (MHD) waves, which are magnetically dominated waves supported by the Sun's pervasive and complex magnetic field. In particular, propagating MHD kink waves have recently been observed to be ubiquitous throughout the solar atmosphere, but, until now, critical details of the transport of the kink wave energy throughout the Sun's atmosphere were lacking. Here, the ubiquity of the waves is exploited for statistical studies in the highly dynamic solar chromosphere. This large-scale investigation allows for the determination of the chromospheric kink wave velocity power spectra, a missing link necessary for determining the energy transport between the photosphere and corona. Crucially, the power spectra contain evidence for horizontal photospheric motions being an important mechanism for kink wave generation in the quiescent Sun. In addition, a comparison with measured coronal power spectra is provided for the first time, revealing frequency-dependent transmission profiles, suggesting that there is enhanced damping of kink waves in the lower corona.

Key words: magnetohydrodynamics (MHD) – Sun: chromosphere – Sun: corona – Sun: photosphere – waves

Online-only material: color figure

1. INTRODUCTION

It has long been proposed that the kinetic energy in stellar convective envelopes is transferred throughout the stellar atmosphere by magnetic fields (Osterbrock 1961; Kuperus et al. 1981; Narain & Ulmschneider 1996; Klimchuk 2006; De Pontieu et al. 2007; Tomczyk et al. 2007; Jess et al. 2009; McIntosh et al. 2011; Wedemeyer-Böhm et al. 2012; Morton et al. 2012). A number of popular theories assume that the horizontal components of the motion of convective granulation, observed at the solar photospheric surface, excite incompressible magnetohydrodynamic (MHD) transversal waves in magnetic flux concentrations (Kuperus et al. 1981; Narain & Ulmschneider 1996; Klimchuk 2006). These incompressible motions can either be perpendicular to the constant magnetic surfaces (i.e., kink modes) or tangential to these surfaces (i.e., torsional Alfvén modes; Erdélyi & Fedun 2007). More recently, advanced analytical and numerical models have used either theoretical turbulent convective spectra (Musielak & Ulmschneider 2002; Fawzy et al. 2002) or velocity power spectra estimated from observations of the solar granulation (Ruderman et al. 1997; Cranmer & van Ballegooijen 2005; Cranmer et al. 2007; Chouduri et al. 1993a, 1993b; Matsumoto & Shibata 2010; Antolin & Shibata 2010) as their input spectrum for generating incompressible waves in stellar atmospheres. These models have had some success in generating the necessary non-thermal energy needed for plasma heating in the atmospheric layers and providing the necessary energy flux for accelerating solar winds. However, it was not clear whether the velocity power spectra derived from the horizontal motions were the physically appropriate input for models. This was in part due to a number of recent observations that demonstrated different incompressible wave excitation mechanisms, e.g., vortices (Wedemeyer-Böhm et al. 2012; Morton et al. 2013) and magnetic reconnection (He et al. 2009). However, previously, the main restriction was the dearth of large-scale observational studies of wave behavior in the various solar atmospheric layers, with which the outputs of these numerical models could be compared.

Understanding the role of MHD wave dynamics in solar plasma heating is crucial, but, until recently, detailed studies have proved challenging. It is only in the last few years that space- and ground-based imaging instruments have achieved the necessary spatial resolution to resolve the incompressible motions of the fine-scale magnetic structure. This has resulted in a wealth of evidence from a wide range of instruments demonstrating that incompressible wave energy is ubiquitous throughout the chromosphere (De Pontieu et al. 2007; Morton et al. 2012; Pereira et al. 2012), transition region (McIntosh et al. 2011), and corona (Tomczyk et al. 2007; McIntosh et al. 2011). MHD kink wave energy estimates from observations hint that the chromospheric fine structure exhibits much more energetic motion than the coronal fine structure (McIntosh et al. 2011; De Pontieu et al. 2007; Tomczyk et al. 2007; Morton et al. 2012). However, no attempt has yet been made to demonstrate the transport of kink wave energy between the different atmospheric layers, which is essential for distinguishing between various heating models. Again, this is in part due to the limited nature of previous wave studies. Here, we provide a major missing link in this problem by determining chromospheric velocity power spectra from observations. This allows for a comparison of the chromospheric power spectra with other velocity power spectra derived at different altitudes in the solar atmosphere. The comparisons reveal the first observational details of kink energy transport through the solar atmosphere.

2. OBSERVATIONS

The hydrogen alpha (Hα) spectral line has proved invaluable for exploration of the magnetically dominated chromosphere

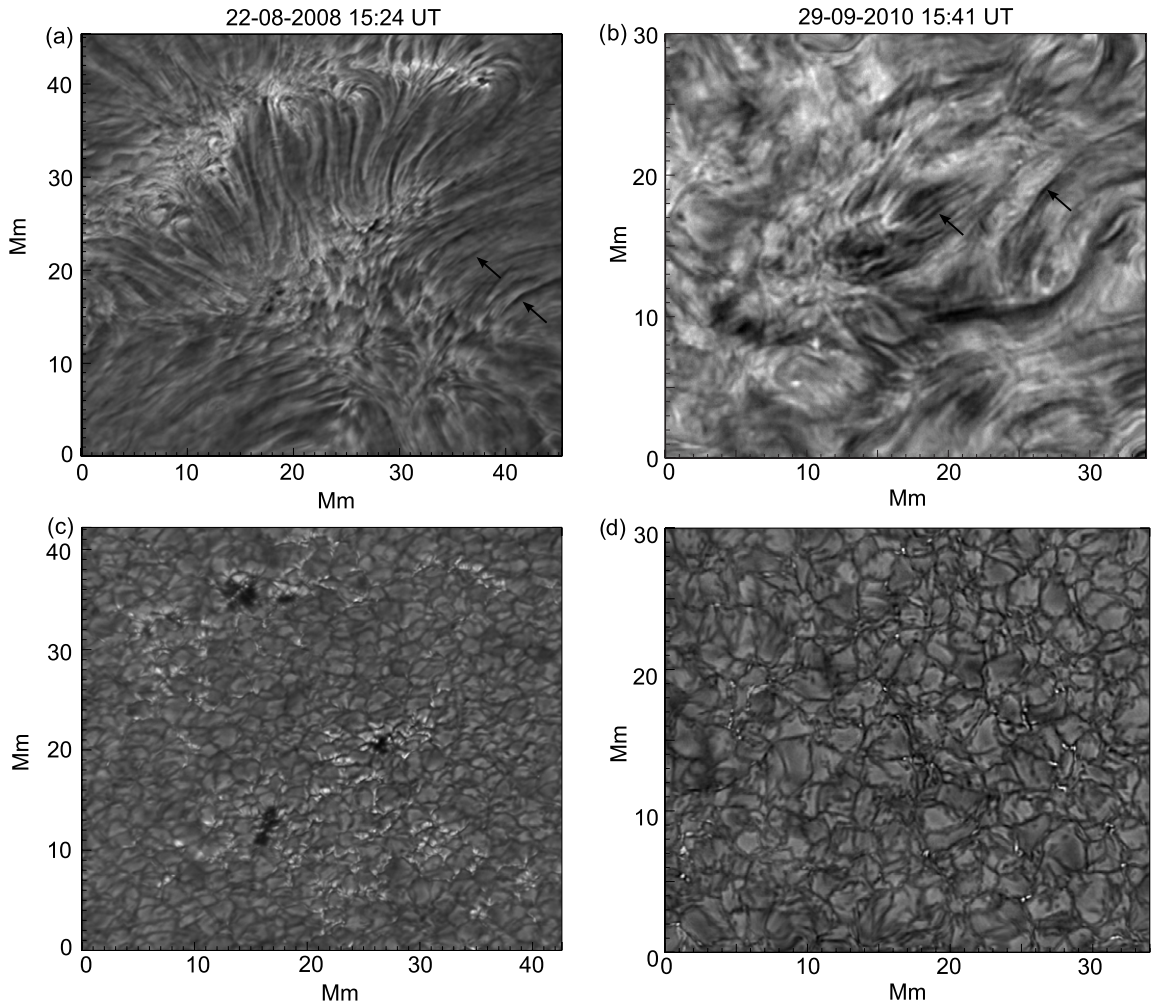

Figure 1. Solar atmosphere observed by ROSA. (a) The solar chromosphere in a magnetically active region, as seen with an Hα filter. The image displays a 45 Mm × 45 Mm sub-region for D1. (b) Hα image of the quiescent solar chromosphere, showing a 34 Mm × 31 Mm sub-region for D2. The existence of fine-scale structuring in the bandpass is evident in both data sets, with both spicules/mottles and cell-spanning fibrils identifiable. Examples of fibrils are highlighted by the black arrows. (c) Corresponding *G*-band image for D1, which reveals magnetic bright points, larger magnetic pores, and the solar granulation. (d) The corresponding *G*-band image for D2, which shows only the magnetic bright points and the granulation. The *G*-band images depict the solar photosphere that lies directly under the Hα chromosphere.

(Rutten 2012), in particular for incompressible wave studies. Here, we use two Hα data sets taken with Rapid Oscillations in the Solar Atmosphere (ROSA; Jess et al. 2010) at the Dunn Solar Telescope (DST) at Sacramento Peak, USA. Both data sets are positioned relatively close to disk center, which implies that the line of sight (LOS) is almost vertically down into the solar atmosphere.

The data sets were obtained at 15:24–16:35 UT on 2008 August 22 (D1) and 15:41–16:51 UT on 2010 September 29 (D2). The first data set (D1) is a magnetically active region located at (N14.8, E40.2). The second data set (D2) is a $69\farcs3 \times 69\farcs1$ region of the quiescent solar atmosphere, positioned close to disk center (N0.9, W6.8). Both data sets were taken with a spatial sampling of $0\farcs069$ pixel^{-1}. During the observations, high-order adaptive optics (Rimmele 2004) were used to correct for wave-front deformations in real time.

The Hα data were sampled at 10 frames s^{-1} for D1 and 2.075 frames s^{-1} for D2. All images were improved by using speckle reconstruction (Wöeger et al 2008). The cadence of the two time series are 6.4 s for D1 and 7.7 s for D2. To ensure accurate co-alignment in all bandpasses, the broadband times series were Fourier co-registered and de-stretched (Jess et al. 2007).

D1 focuses on a region of relatively strong magnetic activity, with the *G*-band images of the photosphere (Figure 1) revealing underlying small (∼200 km diameter; Crockett et al. 2010) bright, intense magnetic elements (Berger & Title 2001) located in the intergranular network and larger (1000 km) dark magnetic pores. In contrast, the *G* band for the second data set (D2) reveals only magnetic bright points, suggesting the total magnetic flux underlying the D2 Hα region is significantly less than in D1. The effect of the differing magnetic fluxes is reflected in the chromospheric features detected in Hα. Here, we are mainly interested in the dark fine structure known as fibrils. Modeling of Hα line formation suggests that the line core intensity is inversely proportional to density, implying that the fibrils are overdense compared with their ambient environment (Leenaarts et al. 2012). A few of these features are highlighted in Figure 1. D1 has very clear, distinct, and ordered fibrillar structures that are long lasting. The fine-scale structure in D2 is, however, less distinct and is not so ordered. However, regions of elongated fibrillar structures that outline the chromospheric magnetic field (Leenaarts et al. 2012) can still be identified. The footpoints of the fibrils appear to be rooted in the regions of intense magnetic field (Reardon et al. 2012), with the other footpoints in intergranular lanes.

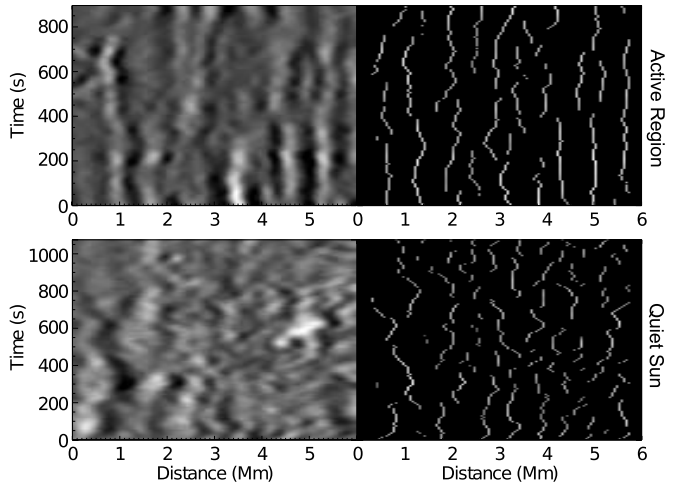

Figure 2. Left panels show example unsharp-masked time–distance diagrams from the active and quiet Sun fibrils. The right-hand panels are the results of the feature tracking algorithm that reveal the displacements of the fibrils.

In Section 4, we make use of results obtained from different instruments. We provide here brief details of the data sets used.

The photospheric velocity power spectrum (red dot-dashed line in Figure 5) was obtained by measuring the motions of granulation using the *Hinode* Solar Optical Telescope *G*-band channel (further details are given in Matsumoto & Kitai 2010). The data were obtained on 2007 March 18 at 07:56 UT. The photospheric velocity power spectrum derived from the data is representative of the quiescent Sun and is comparable to power spectra derived from 13 other data sets.

The other two photospheric power spectra (blue dashed and green solid lines in Figure 5) were obtained by measuring the motions of individual magnetic bright points using the Swedish Solar Telescope (further details are given in Chitta et al. 2012). The data were obtained on 2006 June 18 at 13:10 UT.

The coronal velocity power spectrum was obtained using the Coronal Multi-channel Polarimeter (CoMP) and details are given in Tomczyk & McIntosh (2009). The data were obtained on 2005 October 30.

3. DATA ANALYSIS

On analyzing the Hα movies of these two regions, the dynamic behavior of the chromospheric fine structure is evident. Our interest is directed toward the axial transverse displacement of the chromospheric fibrils, which is the unique signature of MHD kink wave motion. The transverse fibril displacements are identified and measured using a semi-automated tracking mechanism (Morton et al. 2013). We give a brief description here.

The first step in the analysis of the observed transverse waves is to apply an unsharp-mask procedure to the Hα images. Cross cuts are placed perpendicular to the axis of the fibrils and time–distance plots are created, examples of which are shown in Figure 2. The time–distance plots clearly reveal the transverse motions of the fibril structures. For each fibril segment in each time slice, the central pixel is identified and provides the fibril tracks through time. The result is shown in the right-hand panels of Figure 2.

It can be seen that the observed motions are sinusoidal in nature, with one period typically dominating the motion of an individual fibril at a specific time. This mono-periodic behavior is typical of chromospheric transverse waves, although the measurement of many such features at various times and numerous locations shows a rather broad range of frequencies (e.g., Okamoto & De Pontieu 2011; Morton et al. 2013).

The fibril tracks are then fit with a Levenberg–Marquardt non-linear fitting algorithm (*mpfit.pro;*Markwardt 2009). A function of the form

$$F(t) = G(t) + A\sin(\omega t - \phi) \quad (1)$$

is used to fit the oscillations. Here, $G(t)$ is a linear function, A is the displacement amplitude of the oscillation, ω is the frequency, and ϕ is the phase of the oscillation. The fitting algorithm is supplied with the errors on each data point, where it is assumed that the given error is the 1σ uncertainty. The fitting of a sinusoidal function of a single frequency leads to the measurement of the dominant oscillation frequency of the fibril. Residuals exist between the fit and the measured track, which could be the signature of a superposition of different frequencies.

The analyzed fibrils cover the entire field of view for both data sets. In D1 and D2, a total of 744 and 841 sinusoidal transverse displacements are measured, respectively. Histograms of the periods, transverse amplitudes, and velocity amplitudes are given in Figure 3. The previous observations of fibrils (Morton et al. 2012, 2013; Kuridze et al. 2012), off-limb spicules (De Pontieu et al. 2007; Pereira et al. 2012), and other small-scale chromospheric features (Sekse et al. 2012) are found to be consistent with our extensive statistical study here. Note that longer-period waves are observable in magnetically more

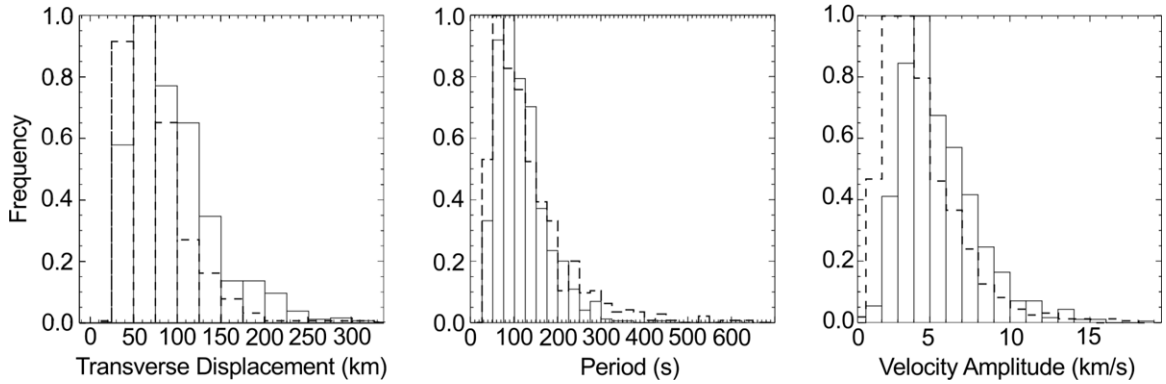

Figure 3. Histograms of measured properties of transverse motions for chromospheric fine structure. The histograms show, from left to right, transverse displacement amplitude, the period, and transverse velocity amplitude. The dashed and solid lines correspond to the results from D1 and D2, respectively. The mean and standard deviations are $P_{D1} = 130 \pm 92$ s, $A_{D1} = 73 \pm 36$ km, $v_{D1} = 4.4 \pm 2.4$ km s^{-1} and $P_{D2} = 116 \pm 59$ s, $A_{D2} = 94 \pm 47$ km, $v_{D2} = 5.5 \pm 2.4$ km s^{-1}.

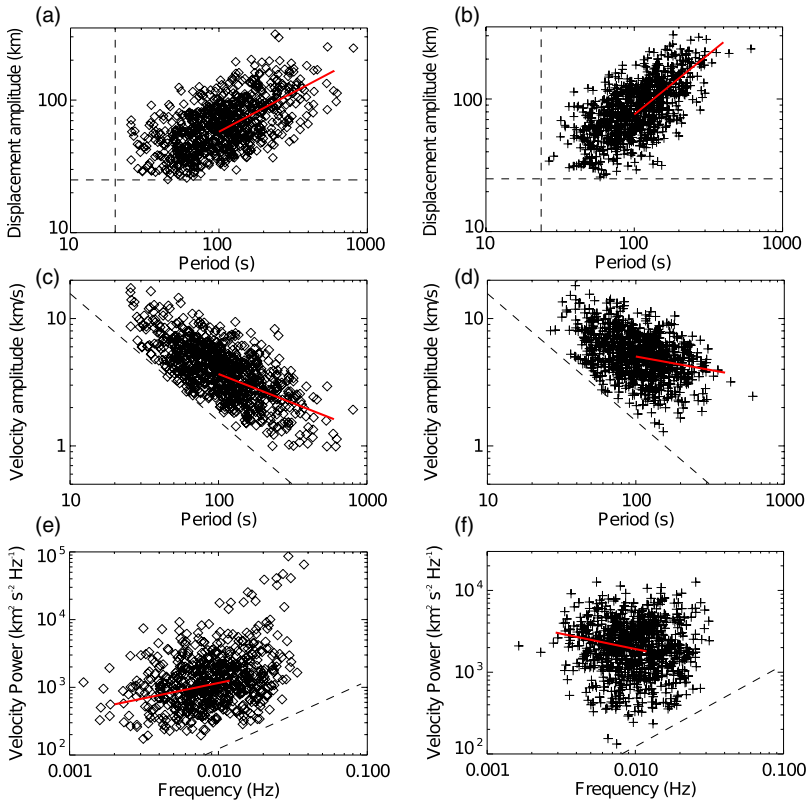

Figure 4. Observed wave properties as functions of period. Scatter plots of the transverse displacement vs. period ((a), (b)), velocity amplitude vs. period ((c), (d)), and the chromospheric power spectrum ((e), (f)) for low-frequency kink waves. The diamonds correspond to the results from the D1 data set and the crosses are the results from D2. The red lines correspond to the weighted power-law fits. The black dashed lines highlight the observational limitations.

(A color version of this figure is available in the online journal.)

active regions than in the quiescent Sun. This is unlikely to be a physical phenomenon but a consequence that the visible lifetimes of the fibrillar structures are longer in the active regions than in the quiescent regions.

Next, we demonstrate how the observed transverse displacements (A) and velocity amplitudes (v) vary as a function of period (Figure 4). In Figures 4(a) and (b), transverse displacement versus period is plotted. The ability to detect waves with certain periods and displacement amplitudes is also subject to observational constraints based on the resolution of the DST and analysis techniques. The fitting technique locates the center of the structure to within one pixel and, hence, has an error of $\pm$25 km (0.5 pixel) on each point, i.e., assuming that the center of the structure was shifted over half a pixel in either direction, the minimum would be located in the neighboring pixel. The fitting algorithm is supplied with the errors on each data point, where it is assumed that the given error is the 1σ uncertainty. The fitting routine then calculates the 1σ error on each fit parameter. Theoretically, we only need three data points to be able to resolve a sinusoidal displacement, hence, the minimum resolvable period is 20 (24) s for data D1 (D2). These limitations correspond to the dashed lines showing the minimum measurable amplitudes and period overplotted in Figure 4(a). The constraining lines suggest, for the shortest measurable periods, the measured distribution of transverse amplitudes is likely influenced by the observational limitations. This effect is reduced for the quiescent Sun data (D2) because the typical measured displacements amplitudes are larger in D2 than in the active region (D1) (see also Figure 3).

To provide a fit to the generated data points, we first note that the transverse displacement shows a lognormal distribution if we project the points onto the displacement axis. We bin the data in the frequency domain, with bins of width 0.001 Hz between 0.004–0.01 Hz and widths of 0.05 Hz between 0.01–0.02 Hz. Data less than 0.004 Hz are placed in one bin and data above 0.02 Hz are placed in another. For each frequency bin, we take the log of the transverse displacement and plot a probability density function (PDF). A Gaussian is fit to each PDF and the centroid gives the median log displacement value while the width provides the standard deviation. It should be borne in mind that the bin for $<$0.004 Hz contains about half the number of data points as the other bins, i.e., it is less reliable. Furthermore, the data points in the bins for frequencies $>$0.01 Hz are subject to larger errors and suffer increased influence from the observational constraints.

The data points generated from the PDFs are then fit with a power law of the form $10^a P^b$ (where P is the period of the wave) computed with a non-linear Levenberg–Marquardt algorithm (Markwardt 2009). The data points are weighted by the standard deviation of each PDF divided by the square root of the number of elements in each distribution, i.e., the standard error. In an attempt to negate the influence of the observational constraints on the results, the fit to the data is only for results with periods longer than 100 s. The fit gives $a = 0.58 \pm 0.15$, $b = 0.59 \pm 0.07$ for D1 and $a = 0.07 \pm 0.12$, $b = 0.91 \pm 0.05$ for D2.

Maximum transverse velocity amplitudes for the kink waves can be obtained from the fit using the relation $v = \omega A$.

For the minimum resolvable velocity amplitude, we calculate the constraint as the minimum displacement amplitude multiplied by 2π and divided by the period.

In Figures 4(c) and (d), velocity amplitude versus period is displayed on a log–log axis. In light of the observational constraints discussed above, the velocity amplitudes are also fit with a power-law from $P = 100$ s onward. The measured power laws for D1 (D2) are $a = 1.48 \pm 0.16$, $b = -0.46 \pm 0.07$($a = 1.12 \pm 0.14$, $b = -0.21 \pm 0.06$). The power of the observational constraint for both data sets is $b = -1$.

As suggested by the fits to the transverse displacements, an increase in velocity amplitude for decreasing period is present. Therefore, this suggests that waves with higher frequency transport a greater amount of energy through the chromosphere than the waves with lower frequency. If this trend was to continue, it would give support to incompressible MHD wave heating theories in which higher frequency waves are the dominant source of the wave energy.

The next, and key, step in the analysis is to estimate the chromospheric velocity power density as a function of frequency ($f = 1/P$) for kink waves (Figures 4(e) and (f)). The one-sided velocity power density, W, for a time series $v(t)$ is given by

$$W = \frac{2(\Delta t)^2 \mid V_n \mid^2}{T}, \quad (2)$$

where V_n are the Fourier coefficients of $v(t)$, Δt is the sample time, $T = N\Delta t$ is the length of the time series, and N is the number of samples. For a time series described by $v(t) = A\omega \sin(\omega t)$, it is found that

$$\frac{\mid v_{\max} \mid^2}{2} \approx 2\frac{\mid V_{\max} \mid^2}{N^2}, \quad (3)$$

where $|V_{\max}|$ is the Fourier coefficient with the largest root mean square value. The left-hand side can be interpreted as the time-averaged value of $v(t)$, i.e.,

$$\frac{\mid v_{\max} \mid}{\sqrt{2}} = \frac{\mid A\omega \mid}{\sqrt{2}},$$

which, for a velocity time series, we denote $\langle v \rangle$. Substituting Equation (3) into Equation (2) and using the relation $\Delta f = 1/(N\Delta t)$, we obtain the following relation for the velocity power:

$$W = \frac{\langle v \rangle^2}{\Delta f} = \frac{v^2}{2\Delta f}. \quad (4)$$

The Δf term acts as a scaling factor that is inversely proportional to the length of time the oscillatory signal is observed for. For the two data sets used in this paper, the lifetime of the measured oscillations is proportional to $1/f$. The observational constraint for the velocity power is then calculated using the form of Equation (3), and is hence given by the time-averaged velocity constraint (i.e., $v/\sqrt{2}$) squared multiplied by $1/f$.

The velocity power is plotted on log–log axes and is subject to a weighted fit of a power-law function of the form $10^a f^b$. Following the previous power-law fits, the fit is calculated for $P > 100$ s ($f < 0.01$ Hz). The power-law fit gives, for D1 (D2), $a = 3.97 \pm 0.54$, $b = 0.45 \pm 0.25$ ($a = 2.53 \pm 0.23$, $b = -0.37 \pm 0.11$). The derived velocity power spectra provide us with a powerful tool that can be applied to compare velocity power spectra established in other layers of the solar atmosphere. Such a comparison can reveal details on the frequency-dependent transport of non-thermal energy through the solar atmosphere.

It should be noted that the given values for velocity power do not include the number density of measured events in frequency space. This is because the observed number of events at low and high frequencies is biased by the fibrils' lifetimes and the limitations of the measurement technique, respectively. Scaling with respect to the number density would then introduce observational biases to the power spectra. In order to assess whether the power spectra are influenced by neglecting the number density, the power spectral density is calculated for the longest time series via a Fourier transform. We find that the gradient of the obtained power spectra is in agreement with that obtained already. Hence, it appears that neglecting the number density of events does not influence the power spectra.

4. DISCUSSION AND CONCLUSIONS

4.1. Wave Generation

It is natural to wonder how MHD kink waves are actually generated. It may be expected that the waves spectra should contain a signature of their excitation mechanism, e.g., the horizontal photospheric motions. On the other hand, wave spectra can be modified due to mode conversion (e.g., Carlsson & Bogdan 2006; Cally & Goossens 2008; Fedun et al. 2011) at altitudes where the Alfvén speed equals the sound speed (thought to be the low chromosphere in the quiet Sun—e.g., Wedemeyer-Böhm et al. 2009), due to reflection from strong gradients in plasma quantities present in the transition region (e.g., Hollweg 1981; Fedun et al. 2011) or non-linear processes associated with turbulent cascade (Cranmer & van Ballegooijen 2005).

Morton et al. (2013) raised the question whether current photospheric power spectra are a suitable input for numerical models of wave heating. The motions of the photospheric footpoints of magnetic fields are typically measured from horizontal motions of magnetic bright points or granular motions. These motions are assumed to displace the whole flux element, with horizontal length scales proportional to the granulation (10^3 km) on the timescales of granular flow patterns (a few minutes). It was suggested in Van Ballegooijen et al. (2011) that additional transverse motions may be generated due to highly turbulent convective downflows (e.g., Vögler et al. 2005). These transverse displacements would occur inside the magnetic elements on length scales shorter then the features ($\sim$100 km) and potentially have shorter associated timescales than the granular motions.

The data points from the generated PDFs are plotted in Figure 5. In addition, the photospheric velocity power spectra, measured from two different characteristic sets of quiescent photospheric phenomena (granulation, Matsumoto & Kitai 2010; magnetic bright points, Chitta et al. 2012), are overplotted. It can be seen from these spectra that there is more power at the lower frequencies and that the power drops off rapidly for timescales less than a few minutes ($\sim$5 mHz). The photospheric results are scaled up by factors of 20–70 for visual clarity. This is simply due to the smaller velocity amplitudes in the solar photosphere. The increase in amplitude from the photosphere to chromosphere is expected because of the decrease in density with height.

The gradient of the chromospheric power spectrum for D1 is relatively steep, showing an increase in velocity power with frequency. The spectra do not appear to show a correlation

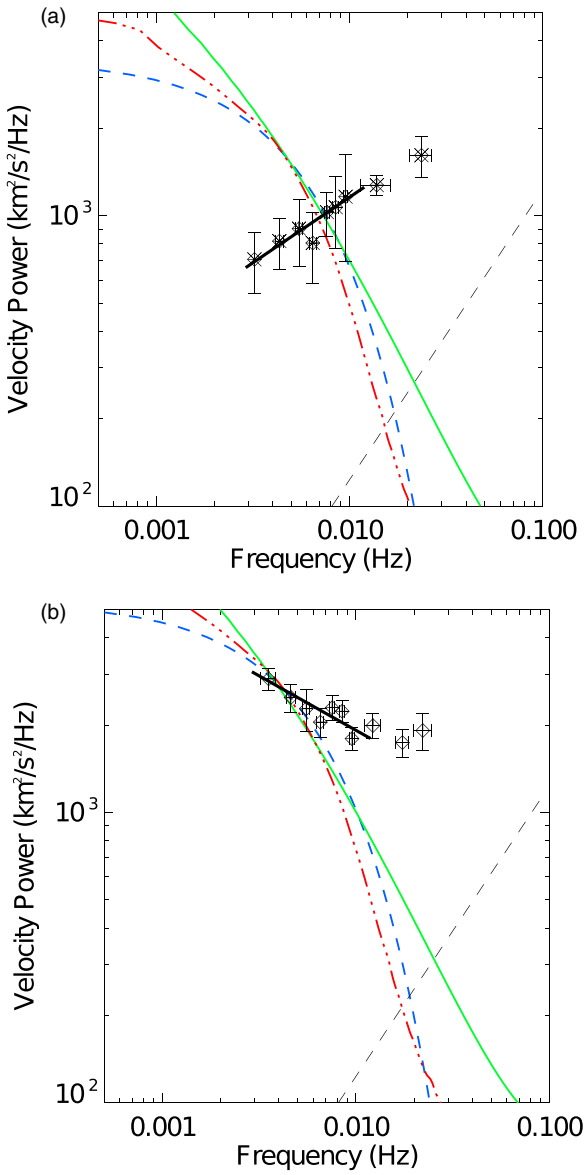

Figure 5. Comparing the power spectra of the photosphere and chromosphere. (a) The figure displays the median velocity power in the chromosphere as a function of frequency for the magnetically active region D1. The velocity power data points are calculated from frequency-binned PDFs and the vertical error bars show the standard deviation of the velocity power in the bins. Overplotted are the photospheric velocity power spectra of horizontal motions (Matsumoto & Kitai 2010: red dot-dashed and Chitta et al. 2012: green solid and blue dashed). The photospheric data have been scaled by a constant factor for comparison. (b) Same as (a), but for the quiescent Sun region D2.

with the photospheric power spectra. The lack of similarity could suggest that photospheric motions are not responsible for the driving of the waves in the active regions. Conversely, the photospheric velocity power spectra are derived for quiescent Sun regions. Photospheric flow measurements (Title et al. 1989) show that flows are suppressed as the magnetic activity increases. This would potentially suppress the power at lower frequencies and hence the photospheric motions in active regions may produce waves with alternate power spectra. To the best of our knowledge, there are no observational horizontal velocity power spectra for magnetically active regions to provide a comparison with.

In contrast to the results for D1, a very good agreement exists between the gradients of the quiescent chromospheric (D2) and photospheric velocity power spectra for waves with $f < 8$ mHz. The correlation indicates that the horizontal photospheric motions are potentially responsible for generating the low-frequency chromospheric dynamics. It is worth noting that the power spectra for low-frequency transverse motions in prominences also display a similar correlation with horizontal photospheric motions (Hillier et al. 2013). There is a flattening of the gradient of the velocity power spectra for frequencies >8 mHz (again seen in prominence wave power spectra). At present, it is not possible to determine the extent to which this result is influenced by observational artifacts (e.g., influence of the observational constraint) and how much additional power is due to genuine physical phenomena. The excess power could potentially be explained if there is an additional source of wave power at short spatial and temporal scales in the photosphere, e.g., turbulent convective downflows (Van Ballegooijen et al. 2011).

Further studies with a combination of higher-cadence, improved spatial resolution, and more advanced wave measurement routines are likely required to resolve this ambiguity. As noted in Hillier et al. (2013), further work is required to establish a direct cause and effect relationship between the horizontal motions and the transverse waves observed higher in the solar atmosphere, e.g., via the inclusion of phase spectra, which will be the aim of future studies.

4.2. Wave Damping

Let us now compare the chromospheric power spectrum with those derived for the corona (Tomczyk & McIntosh 2009). The underlying assumption has to be made that the coronal observations taken by CoMP and the ROSA observations both give results typical of quiescent Sun phenomena for the corona and chromosphere, respectively. We note that the CoMP data are also of a quiescent Sun region. Large, faint loop structures are barely visible in CoMP and *Solar and Heliospheric Observatory* 195 Å images. Examining the region as it rotates onto the disk reveals no visible signs of large magnetic flux concentrations in *Solar and Heliospheric Observatory* magnetograms. Hence, we assume that the region is also typical of the quiescent Sun. However, we note that the general magnetic topology throughout the solar corona could well be different between the two data sets. This is because the ROSA data are taken further into the solar cycle than the CoMP data.

Figure 6(a) shows the velocity power measured with CoMP for a coronal loop arcade structure divided by the fitted power law for the chromospheric velocity power from region D2, for the period range 100–500 s. The ratio reveals that the velocity power appears to decrease significantly from the chromosphere to the corona, with the power of the high-frequency waves decreasing to a much greater degree. The velocity power of the CoMP data is, however, averaged over a distance of 250 Mm along a coronal loop system, where frequency-dependent wave damping has occurred (Tomczyk & McIntosh 2009; Verth et al. 2010). However, for our purposes, it is necessary to calculate the input velocity power at the base of the coronal loop system. The minimum height in the solar atmosphere that CoMP can measure Doppler velocities is ~20 Mm above the solar surface. The input power spectra at the base of the CoMP loop system (at a height of 20 Mm) can be determined by exploiting the measured damping rates (Verth et al. 2010).

First, the spatially averaged total power as a function of frequency, f, is denoted by $\langle P(f)\rangle_{\rm Total}$. This averaged velocity power detected by CoMP is composed of waves propagating both upward and downward along the loop path. The particular

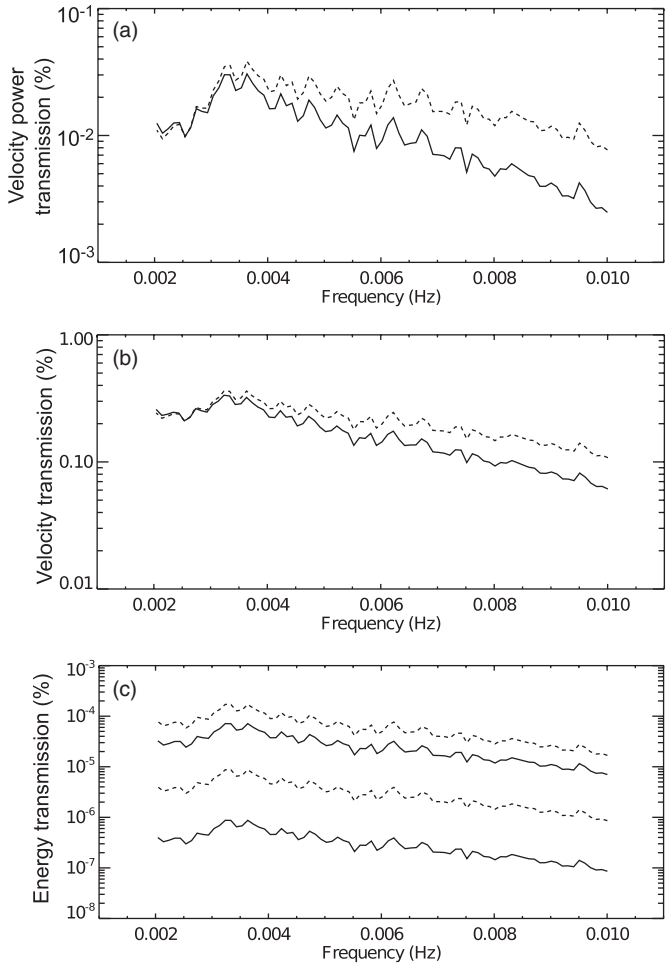

Figure 6. Transmission profiles from the chromosphere to the corona. A comparison of kink waves in the quiescent corona observed with CoMP and the quiescent chromosphere (D2). (a) The ratio of coronal velocity power to chromospheric velocity power. (b) The ratio of coronal velocity amplitude to chromospheric velocity amplitude. The solid lines are the ratios using the spatially averaged CoMP measurements. The dashed lines correspond to the ratio using the estimated input power/velocity in the corona at a height of 20 Mm. (c) The ratio of coronal integrated total wave energy to chromospheric integrated total wave energy (solid lines) and the ratio of coronal integrated Poynting flux to chromospheric integrated Poynting flux (dashed lines). The two lines for each quantity correspond to the maximum and minimum ratios possible, reflecting the uncertainty in known values of plasma parameters.

averaged velocity power of the waves that propagate from the loop base, $s = 0$, to the loop apex, $s = L$, is denoted $\langle P(f)\rangle_{\rm up}$. The averaged velocity power of waves propagating downward along the loop path is denoted $\langle P(f)\rangle_{\rm down}$. These latter waves will have been generated at the other loop footpoint so once they reach the apex they will have already traveled a distance L. The spatially averaged total power is then given by

$$\langle P(f)\rangle_{\rm Total} = \langle P(f)\rangle_{\rm up} + \langle P(f)\rangle_{\rm down}. \quad (5)$$

Now, modeling the observed damping (Tomczyk & McIntosh 2009) of the waves as they propagate between the loop base, $s = 0$, and the loop apex, $s = L$, the averaged total velocity power is given by

$$\langle P(f)\rangle_{\rm Total} = \frac{1}{L}\int_0^L P(f)_{\rm in}\exp\left(-\frac{2s}{L_D}\right)ds + \frac{1}{L}\int_L^{2L} P(f)_{\rm in}\exp\left(-\frac{2s}{L_D}\right)ds, \quad (6)$$

where $P_{\rm in}(f)$ is the power input at the CoMP base height (i.e., 20 Mm), $L_D = (\tau/P)(c_k/f)$ is the damping length, c_k is the kink wave phase speed, and τ/P is the quality factor (Verth et al. 2010). Integrating and re-arranging gives

$$P(f)_{\rm in} = \frac{2L}{L_D}\langle P(f)\rangle_{\rm Total}\left[1-\exp\left(-\frac{4L}{L_D}\right)\right]^{-1}. \quad (7)$$

Supplementing Equation (7) with $c_k = 0.6$ Mm s^{-1} (Tomczyk & McIntosh 2009), $\tau/P = 2.69$ (Verth et al. 2010), and $L = 250$ Mm, we determine the dashed lines in Figure 6(a).

The gradient for the frequency dependent trend is now shallower but still gives about a factor of five decrease in velocity power for the higher-frequency waves ($f \approx 10$ mHz) relative to the lower-frequency waves ($f \approx 2$ mHz). This behavior is also shown for the transmission profile of the velocity amplitude in Figure 6(b), where the decrease in velocity amplitude is about a factor of three over this frequency range.

We now determine the energy loss between the chromosphere and corona. The following relations show the time-averaged, spatially integrated total energy (E) and Poynting flux (S_z) for MHD kink waves (Goossens et al. 2013):

$$E = (\rho_i + \rho_e)v_r^2\pi R^2, \quad S_z = (\rho_i + \rho_e)v_r^2 c_k \pi R^2, \quad (8)$$

where

$$c_k^2 = \frac{B_i^2 + B_e^2}{\mu_0(\rho_i + \rho_e)} \quad (9)$$

is the phase (propagation) speed of the wave, ρ is the density, v_r is the velocity perturbation, μ_0 is the magnetic permeability of free space, and R is the radius of the flux tube. The subscripts refer to the internal, i, and ambient, e, plasma quantities.

Due to significant uncertainties in the values of the equilibrium plasma parameters, we calculate the minimum and maximum ratios possible for both quantities. In general, estimates of density are 10^{-12}–10^{-13} kg m^{-3} in the corona (Warren & Brooks 2009) and 10^{-9}–10^{-11} kg m^{-3} for the chromosphere (Beckers 1968). The measured radii of flux tubes in the chromosphere are 100–400 km (Morton et al. 2012), while measurements from TRACE (Watko & Klimchuk 2000) and Hi-C (Morton & McLaughlin 2013) suggest 100–1000 km for coronal loops. Finally, measured phase speeds of kink waves in the chromosphere suggest the waves propagate at 100–250 km s^{-1} (Morton et al. 2012; Okamoto & De Pontieu 2011) and 600–1000 km s^{-1} in the corona (Tomczyk & McIntosh 2009). The parameters of density, magnetic field, phase speed, and tube radius are height dependent. Physically, this means the values have to satisfy the following relations:

$$\frac{c_{k1}}{c_{k2}} = \sqrt{\frac{\rho_2(1+\chi_2)}{\rho_1(1+\chi_1)}}\frac{B_1}{B_2}, \quad \frac{R_1}{R_2} = \sqrt{\frac{B_2}{B_1}},$$

$$B_1 \leqslant B_2, \quad \rho_1 \leqslant \rho_2.$$

Here, the subscripts 1, 2 refer to the coronal and chromospheric values, respectively, $\chi = \rho_e/\rho_i = 0.1$–$0.5$, and we assume $B_i \approx B_e$. The second of these equations is derived from the conservation of magnetic flux, the third assumes that the magnetic field strength does not increase with height, and the fourth assumes that density does not increase with height.

In Figure 6(c), the ratio of the integrated total energy and integrated Poynting flux between the corona and the chromosphere are shown.

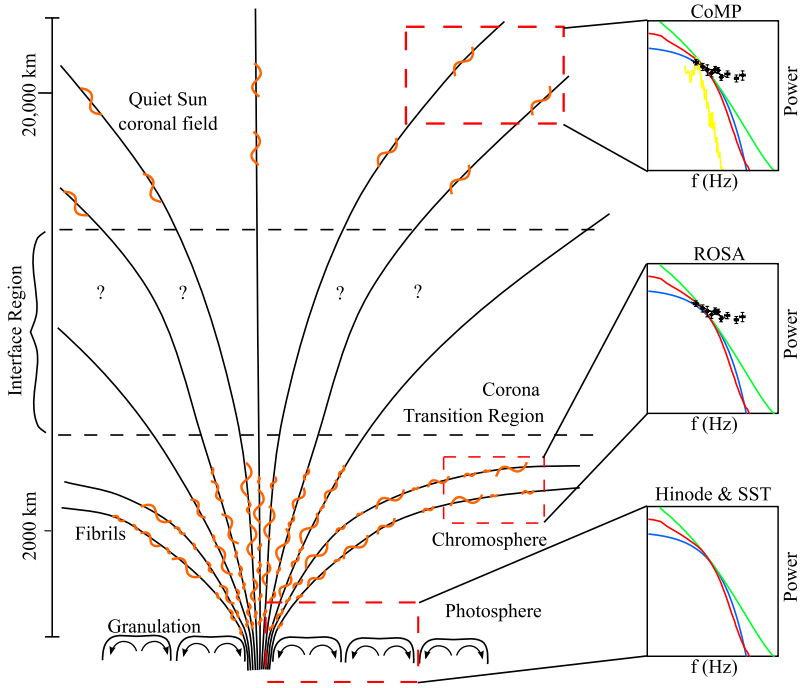

Figure 7. Transport of energy through the quiescent solar atmosphere; a schematic diagram depicting the transport of kink MHD wave energy through the solar atmosphere, as implied by observational results. The kink MHD waves are assumed to be generated by the horizontal granular motions, which impart a particular power spectra on the waves. Kink MHD waves observed in the quiescent chromosphere demonstrate a similar power spectrum, suggesting that the granular motions have indeed excited them. The waves then enter a region that is difficult to observe with current solar instrumentation. We refer to this as the interface region and it consists of the transition region and low corona. On reaching the upper corona, CoMP measurements reveal that there has been a significant loss of higher-frequency wave energy between the chromosphere and corona. It could well be that the energy has been dissipated and is heating the solar atmosphere.

Figure 6(c) demonstrates that even the upper bound of the ratio suggests only a transmission of 0.01% of the total chromospheric kink wave energy and Poynting flux. These findings come with the following caveat: the spatial sampling (≈4.5 Mm) of CoMP means it may not resolve the coronal fine structure adequately. It has been demonstrated that the effect of LOS integration on multiple unresolved loops leads to an underestimate of kink wave velocity amplitude (De Moortel & Pascoe 2012; De Pontieu & McIntosh 2012). At present, we cannot give an explicit value of CoMPs under-resolution; therefore, Figure 6 represents the transmission profiles of the velocity power, amplitude, etc., rather than the absolute values of the transmission coefficients. We point out that non-thermal widths from the CoMP observations are much larger (30–40 km s^{-1}) than the Doppler shifts and may provide a better indicator of the amplitudes of the unresolved kink motions. However, the non-thermal widths are likely to also include contributions from the LOS components of torsional motions, flows, slow waves, magneto-acoustic waves, etc., which complicate their interpretation.

The observed frequency-dependent trends of the quantities in Figure 6 can be explained by frequency-dependent damping, which has been well studied in the case of kink wave damping in coronal loops (Verth et al. 2010; Verwichte et al. 2013). From observations of such damped standing kink waves, the ratio of damping time (τ) over the period provides the relative strength of the damping mechanism, i.e., the quality factor. Statistical studies show coronal values of $\tau/P \approx$ 1–5, meaning the observed kink waves lie in the underdamped regime (Verwichte et al. 2013). In the case of propagating waves, the equivalent measure is L_D/λ, where L_D is the damping length and λ is the wavelength (Terradas et al. 2010). Analysis of damped propagating kink waves detected in the CoMP data reveal that the two measures are in agreement (Verth et al. 2010), i.e., $\tau/P \sim L_D/\lambda$. Assuming that frequency-dependent damping also occurs in the interface region between ROSA and CoMP observations, with $L_D = (\tau/P)c_k/f$, where c_k is the kink wave phase speed, we can estimate the interface region damping lengths using the following relation:

$$P_{\mathrm{out,IR}}(f) \propto P_{\mathrm{in,IR}}(f) \exp\left(-\frac{2L}{L_D}\right), \tag{10}$$

where $P_{\mathrm{out,IR}}(f)$ is the output power from the interface region to the corona (i.e., the CoMP footpoint power spectrum) and $P_{\mathrm{in,IR}}(f)$ is the input power from the chromosphere to the interface region (i.e., the ROSA power spectrum). Writing $L_D = \alpha/f$, where $\alpha = (\tau/P)c_k$, and using estimates of the height of the interface region, i.e., L = 15–20 Mm, we find $\alpha_{\mathrm{IR}} \approx 0.2$ Mm s^{-1} provides a reasonable approximation of the change in gradient between ROSA and CoMP velocity power spectra.

From the analysis of the damping of propagating coronal kink waves $\alpha_{\mathrm{corona}} \approx 1.6$ Mm s^{-1} (Verth et al. 2010), it follows that the damping length in the interface region is about 13% of the estimated coronal damping length. The quality factors in the interface region and corona are related by the following equation:

$$\left(\frac{\tau}{P}\right)_{\mathrm{IR}} = \left(\frac{\alpha}{c_k}\right)_{\mathrm{IR}} \left(\frac{c_k}{\alpha}\right)_{\mathrm{corona}} \left(\frac{\tau}{P}\right)_{\mathrm{corona}}. \tag{11}$$

To estimate $(\tau/P)_{\mathrm{IR}}$ from Equation (11), the previous values are used for α_{IR}, α_{corona}, and $c_{k,\mathrm{corona}}$. $c_{k,\mathrm{IR}} \approx 150$ km s^{-1} is taken for the average phase speed in the interface region (between heights of 5 and 20 Mm; McIntosh et al. 2011)

and $(\tau/P)_{\rm corona} = 2.69$. This gives $(\tau/P)_{\rm IR} \approx 1.35$, about 50% of the coronal value. Hence, the observed trend implies that there is much stronger frequency-dependent kink wave damping in the lower solar corona. Critical damping occurs when $(\tau/P) = 1/(2\pi) \approx 0.16$, so although the estimated quality factor in the interface region is about a half of that in the corona, it is still above the critical damping regime. This is consistent with the fact that these propagating waves are actually observed at higher altitudes with CoMP, i.e., they are not completely killed off within the interface region. The intimation of enhanced and frequency-dependent kink wave damping between the chromosphere and corona has potentially important implications for numerous coronal-heating models, which demonstrate that incompressible wave energy is more efficiently converted to heat at higher frequencies. Furthermore, the particular location of enhanced kink wave damping is significant because there is mounting observational evidence for the chromosphere and interface region being predominant locations for plasma heating processes in the solar atmosphere (Aschwanden et al. 2007; Tripathi et al. 2012).

The results presented here show that the measurement of velocity power spectra provides a very powerful and practical mechanism for analyzing MHD kink wave propagation through the magnetized solar atmosphere. Comparing the velocity power spectra obtained at different altitudes of the atmosphere allows for the possible signatures of kink wave driving and damping to be observed (Figure 7). The picture implied by the observations presented here suggests a qualitative agreement with theoretical expectations for wave propagation through the quiescent solar atmosphere (e.g., Chouduri et al. 1993a; Cranmer & van Ballegooijen 2005), i.e., magnetic waves are driven by the horizontal motions that propagate into the upper solar atmosphere, with the flow of wave energy hindered by the strong gradients present in the transition region.

These observational results do not tell the complete picture though and they raise a number of key questions that need to be answered, e.g., what is the fate of the high-frequency wave energy observed in the chromosphere? What mechanism(s) have led to their decrease in power before they reach the corona? One possible explanation for coronal kink wave damping is based on mode conversion to $m = 1$ torsional Alfvén waves at resonant magnetic surfaces naturally present across inhomogeneous solar atmospheric waveguides. Such a process could also explain the stronger kink wave damping in the interface layer (the 15–20 Mm region linking between ROSA and CoMP observations). In the lower atmosphere (at heights of less than 10 Mm), it has recently been shown that torsional Alfvén and kink waves are concurrent in spicules (De Pontieu et al. 2012), providing evidence that mode coupling is already happening at sub-interface region heights. To fully understand the interaction and evolution of these coupled incompressible MHD wave modes in the interface layer between the chromosphere and corona, missions such as the Interface Region Imaging Spectrometer will be crucial.

R.E. acknowledges M. Kéray for patient encouragement. A.H. is supported by the Grant-in-Aid for Young Scientists (B, 25800108). The authors are also grateful to the NSF, Hungary (OTKA, Ref. No. K83133), and the Science and Technology Facilities Council (STFC), UK. G.V. acknowledges the Leverhulme Trust. R.M. acknowledges Northumbria University for the award of the Anniversary Research Fellowship and the Royal Astronomical Society for the award of travel grants. Observations were obtained at the National Solar Observatory, operated by the Association of Universities for Research in Astronomy, Inc. (AURA), under agreement with the National Science Foundation. We would like to thank the technical staff at the DST for their help and support during the observations. Further thanks are required for M. Mathioudakis, D. B. Jess, and Queen's University Belfast, UK for ROSA support and S. Tomczyk, T. Matsumoto, and L. P. Chitta, who provided us with the results from other instruments

REFERENCES

Antolin, P., & Shibata, K. 2010, ApJ, 712, 494
Aschwanden, M. J., Winebarger, A. R., Tsiklauri, D., & Peter, H. 2007, ApJ, 659, 1673
Beckers, J. M. 1968, SoPh, 3, 367
Berger, T. E., & Title, A. M. 2001, ApJ, 533, 449
Cally, P. S., & Goossens, M. 2008, SoPh, 251, 251
Carlsson, M., & Bogdan, T. J. 2006, RSPTA, 364, 395
Chitta, L. P., van Ballegooijen, A. A., Rouppe van der Voort, L., DeLuca, E. E., & Kariyappa, R. 2012, ApJ, 752, 48
Chouduri, A. R., Affuet, H., & Priest, E. R. 1993a, SoPh, 143, 49
Chouduri, A. R., Dikpati, M., & Banerjee, D. 1993b, ApJ, 413, 811
Cranmer, S. R., & van Ballegooijen, A. A. 2005, ApJS, 156, 265
Cranmer, S. R., van Ballegooijen, A. A., & Edgar, R. J. 2007, ApJS, 171, 520
Crockett, P. J., Mathioudakis, M., Jess, D. B., et al. 2010, ApJL, 722, L188
De Moortel, I., & Pascoe, D. J. 2012, ApJ, 746, 31
De Pontieu, B., Carlsson, M., Rouppe van der Voort, L. H. M., et al. 2012, ApJL, 752, L12
De Pontieu, B., & McIntosh, S. W. 2012, ApJ, 761, 138
De Pontieu, B., McIntosh, S. W., Carlsson, M., et al. 2007, Sci, 318, 1574
Erdélyi, R., & Fedun, V. 2007, Sci, 318, 1572
Fawzy, D., Ulmschneider, P., Stępień, K., Musielak, Z. E., & Rammacher, W. 2002, A&A, 386, 983
Fedun, V., Shelyag, S., & Erdélyi, R. 2011, ApJ, 727, 17
Goossens, M., Van Doorsselaere, T., Soler, R., & Verth, G. 2013, ApJ, 771, 74
He, J., Marsch, E., Tu, C., & Tian, H. 2009, ApJL, 705, L217
Hillier, A., Morton, R. J., & Erdélyi, R. 2013, ApJL, 779, L16
Hollweg, J. V. 1981, SoPh, 70, 25
Jess, D. B., Mathioudakis, M., Christian, D. J., et al. 2010, SoPh, 261, 363
Jess, D. B., Mathioudakis, M., Erdélyi, R., et al. 2009, Sci, 323, 1582
Jess, D. B., McAteer, R. T. J., Mathioudakis, M., et al. 2007, A&A, 476, 971
Klimchuk, J. A. 2006, SoPh, 234, 41
Kuperus, M., Ionson, J. A., & Spicer, D. S. 1981, ARA&A, 19, 7
Kuridze, D., Morton, R. J., Erdélyi, R., et al. 2012, ApJ, 750, 51
Leenaarts, J., Carlsson, M., & Rouppe van der Voort, L. 2012, ApJ, 749, 136
Markwardt, C. B. 2009, in ASP Conf. Ser. 411, Astronomical Data Analysis Software and Systems XVIII, ed. D. A. Bohlender, D. Durand, & P. Dowler (San Francisco, CA: ASP), 251
Matsumoto, T., & Kitai, R. 2010, ApJL, 716, L19
Matsumoto, T., & Shibata, K. 2010, ApJ, 710, 1857
McIntosh, S. W., de Pontieu, B., Carlsson, M., et al. 2011, Natur, 475, 477
Morton, R. J., & McLaughlin, J. A. 2013, A&A, 533, L10
Morton, R. J., Verth, G., Fedun, V., Shelyag, S., & Erdélyi, R. 2013, ApJ, 768, 17
Morton, R. J., Verth, G., Jess, D. B., et al. 2012, NatCo, 3, 1315
Musielak, Z. E., & Ulmschneider, P. 2002, A&A, 386, 606
Narain, U., & Ulmschneider, P. 1996, SSRv, 757, 453
Okamoto, T. J., & De Pontieu, B. 2011, ApJL, 736, L24
Osterbrock, D. E. 1961, ApJ, 134, 347
Pereira, T. M., De Ponteiu, B., & Carlsson, M. 2012, ApJ, 759, 18
Reardon, K. P., Wang, Y. M., Muglach, K., & Warren, H. P. 2012, ApJ, 742, 119
Rimmele, T. R. 2004, Proc. SPIE, 5490, 34
Ruderman, M., Berghmans, D., Goossens, M., & Poedts, S. 1997, A&A, 320, 305
Rutten, R. J. 2012, RSPTA, 370, 3129
Sekse, D. H., Rouppe van der Voort, L. H. M., & De Pontieu, B. 2012, ApJ, 752, 108
Terradas, J., Goossens, M., & Verth, G. 2010, A&A, 524, A23
Title, A. M., Tarbell, T. D., Topka, K. P., et al. 1989, ApJ, 336, 475
Tomczyk, S., & McIntosh, S. W. 2009, ApJ, 697, 1384
Tomczyk, S., McIntosh, S. W., Keil, S. L., et al. 2007, Sci, 317, 1192
Tripathi, D., Mason, H. E., Del Zanna, G., & Bradshaw, S. J. 2012, ApJL, 754, L4
van Ballegooijen, A. A., Asgari-Targhi, M., Cranmer, S. R., & DeLuca, E. E. 2011, ApJ, 736, 3

Verth, G., Terradas, J., & Goossens, M. 2010, ApJL, 718, L102
Verwichte, E., van Doorsselaere, T., White, R. S., & Antolin, P. 2013, A&A, 552, 138
Vögler, A., Shelyag, S., Schüssler, M., et al. 2005, A&A, 427, 335
Warren, H. P., & Brooks, D. H. 2009, ApJ, 700, 762
Watko, J. A., & Klimchuk, J. A. 2000, SoPh, 193, 77
Wedemeyer-Böhm, S., Lagg, A., & Nordlund, Å. 2009, SSRv, 144, 317
Wedemeyer-Böhm, S., Scullion, E., Steiner, O., et al. 2012, Natur, 486, 505
Wöger, F., von der Lühe, O., & Reardon, K. 2008, A&A, 488, 375